ISSN 1063-7788, Physics of Atomic Nuclei, 2008, Vol. 71, No. 12, pp. 2074–2086. © Pleiades Publishing, Ltd., 2008.
Original Russian Text © G.A. Akopdzhanov, V.B. Anikeev, V.A. Bezzubov, I.A. Vasilyev, Yu.V. Gilitsky, S.N. Gurzhiev, S.P. Denisov, A.A. Durum, S.A. Zvyagintsev, A.V. Kozelov, E.A. Kozlovsky, V.M. Korablev, V.I. Koreshev, V.I. Kurbakov, V.V. Lipaev, V.A. Onuchin, A.M. Rybin, Yu.M. Sapunov, M.M. Soldatov, D.A. Stoyanova, K.I. Trushin, A.A. Schukin, V.I. Yakimchuk, 2008, published in Yadernaya Fizika, 2008, Vol. 71, No. 12, pp. 2108–2121.

ELEMENTARY PARTICLES AND FIELDS
Experiment

Study of $K^{\pm} \to e^{\pm}\nu\pi^0$ Decays at the KMN Setup

G. A. Akopdzhanov, V. B. Anikeev, V. A. Bezzubov, I. A. Vasilyev, Yu. V. Gilitsky, S. N. Gurzhiev, S. P. Denisov, A. A. Durum, S. A. Zvyagintsev, A. V. Kozelov, E. A. Kozlovsky, V. M. Korablev, V. I. Koreshev, V. I. Kurbakov, V. V. Lipaev, V. A. Onuchin, A. M. Rybin, Yu. M. Sapunov†, M. M. Soldatov, D. A. Stoyanova, K. I. Trushin, A. A. Schukin, and V. I. Yakimchuk

Institute for High Energy Physics, Protvino, Moscow oblast, 142280 Russia

Received February 8, 2008; in final form, June 24, 2008

Abstract—$K^{\pm} \to e^{\pm}\nu\pi^0$ decays have been studied using the KMN setup at the Institute for High Energy Physics (Protvino). The experiment has been performed in the 36-GeV/c hadron beams of the IHEP accelerator. The accumulated data allow us to select $\sim$1.08M candidates for K_{e3} decays. Analyzing the Dalitz plot of these events, we estimate the linear slope of the charge form factor to be $\lambda_+ = [30.44 \pm 0.83(\text{stat.}) \pm 0.74(\text{syst.})] \times 10^{-3}$.

PACS numbers: 13.20.Eb, 13.20.-v
DOI: 10.1134/S1063778808120089

1. INTRODUCTION

Semileptonic kaon decays still draw the attention of experimenters' by making it possible not only to observe special features of the electromagnetic and weak interactions at low energies but also to reveal manifestation of some other interactions [1–6]. Generally, the decay matrix element K_{l3} is expressed as follows [7]

$$M = \frac{G_{\rm F}\sin\theta_{\rm C}}{\sqrt{2}}\bar{u}(p_\nu)(1+\gamma^5) \tag{1}$$
$$\times \left\{ m_K f_S - \frac{1}{2}[(P_K+P_\pi)_\alpha f_+ \right.$$
$$\left. + (P_K-P_\pi)_\alpha f_-]\gamma^\alpha + \frac{f_T}{m_K}\sigma_{\alpha\beta}P_K^\alpha P_\pi^\beta \right\} v(p_l).$$

Here, the form factors f_S, $f_\pm$, and f_T are functions of the squared four-momentum transferred to leptons $t = (P_K - P_\pi)^2$.

The density of the K_{l3} decay events on the Dalitz plot can be found using Eq. (1), which yields

$$\rho^{K_{l3}}(E_\pi, E_l) \sim |M|^2 \tag{2}$$
$$= A|V|^2 + B\mathrm{Re}(V^*S) + C|S|^2,$$

where E_π and E_l are the pion and lepton energies calculated in the rest frame of decaying kaon. The functions in Eq. (2) which depend on the kinematic parameters of the decay particles are as follows [8]:

$$V = f_+ + \frac{m_l}{m_K}f_T,$$
$$S = f_S + \frac{m_l}{2m_K}f_- + \frac{1}{m_K}\left[(E_\nu - E_l) + \frac{m_l^2}{2m_K}\right]f_T,$$
$$A = m_K(2E_lE_\nu - m_K\Delta E_\pi) - m_l^2\left(E_\nu - \frac{1}{4}\Delta E_\pi\right),$$
$$B = m_l m_K(2E_\nu - \Delta E_\pi),$$
$$C = m_K^2\Delta E_\pi,$$

where

$$\Delta E_\pi = E_\pi^{\max} - E_\pi, \qquad E_\pi^{\max} = \frac{m_K^2 + m_\pi^2 - m_l^2}{2m_K},$$

E_ν is the neutrino energy, and the following parameterization of the vector form factor is adopted [7]:

$$f_+ = f_+(0)\left[1 + \lambda\frac{t}{m_\pi^2} + \lambda'\Big(\frac{t}{m_\pi^2}\Big)^2\right]. \tag{3}$$

In the analysis of K_{e3} decay, the terms proportional to power of the ratio m_e/m_K in Eq. (2) are usually neglected because these values are on the order of 10^{-3} or less.

We transformed the analytical calculations for radiation corrections to K_{e3} decays proposed in [9] into program codes, which were tuned and verified using the numerical data [9, 10]. The values of corrections

†Deceased.

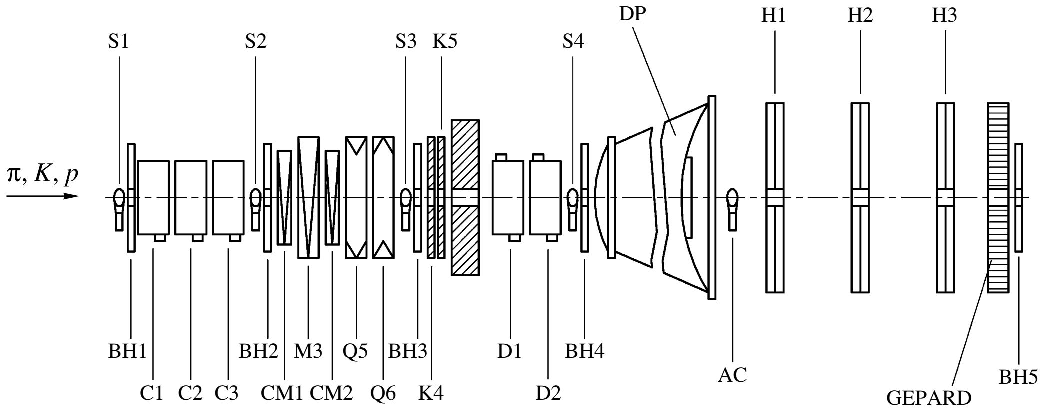

Fig. 1. Layout of the experimental setup: (M) magnets; (Q) quadrupole lenses; (CM) correcting magnets; (K) collimators; (S) scintillation counters; (C, D) threshold and differential Cherenkov counters, respectively; (BH) beam hodoscopes; (DP) evacuated pipe; (AC) anticoincidence counter; (H) scintillation hodoscopes; (GEPARD) electromagnetic calorimeter.

fell within the limits of the calculation accuracy stated in the cited articles throughout the kinematic region of K_{e3} decay.

Within the meson dominance model (the pole model, e.g., see [11]), the t dependence of the form factor is usually associated with the $K^*(890)$ exchange dominance resulting in the following estimate: $\lambda_+ = (m_\pi/m_{K^*})^2$. The slopes of the vector form factor somewhat differ in semileptonic K_{e3} decays of neutral and charged kaons due to a difference in the masses of charged and neutral pions.

2. KMN SETUP

The experiment was carried out on the KMN setup (IHEP, Protvino) [12–14], which is shown schematically in Fig. 1. To study $K^{\pm}$-meson decays, we used hadron beams with momentum about 36 GeV/c, which were produced by 70-GeV protons extracted from the U-70 accelerator on an external aluminum target 7 mm in diameter and 300 mm long. Two dipole magnets and six quadrupole ones located behind of the target comprise channel no. 23 [15] which allows us to extract particles with energies between 10 and 38 GeV/c produced on the target.

The mean hadron flux in the beamline was 4×10^6 per accelerator spill of 1.7 s. We used scintillation counters $S1$–$S4$ and beam hodoscopes BH1–BH4 to monitor the beam intensity and to measure beam particle trajectories. Additionally, the signals from $S1$–$S4$ were used to form the Level-1 trigger.

$K^{\pm}$ mesons were identified with three threshold ($C1$–$C3$) and two differential ($D1, D3$) gas Cherenkov counters. The admixture of other particles in the K-meson peak was far below 1% at the operating pressure [12]. In addition, the threshold counters enabled us to mark electrons in the 10-GeV/c beam and used them to calibrate the GEPARD electromagnetic calorimeter. For this purpose, two beam-bending magnets, which allowed scanning each GEPARD cell, were mounted instead of the differential counters.

Using the BH1–BH4 beam scintillation hodoscopes, it was possible to measure the angles and the coordinates of the charged particle tracks at the entrance to the evacuated "decay pipe" (DP) 58.5 m long; only kaons decayed inside DP ($\sim$20%) were used in further analysis. The pipe flanges had thin Mylar windows across the beam. The exit flange 3.6 m in diameter was manufactured from stainless steel 4 mm thick ($0.23X_0$). The probability of the conversion of a high-energy γ-quantum into an e^+e^--pair in this flange is $\sim$16%.

Undecayed kaons were detected by an anticoincidence scintillation counter AC. In order to accurately measure the position of the beam passing through the whole setup, the BH5 beam hodoscope operating in the counting mode was mounted behind the calorimeter.

The products of kaon decays were detected by three scintillation hodoscopes $H1$–$H3$ and the GEPARD calorimeter. Each hodoscope had two octagonal planes with a distance of 3.85 m between their opposite sides. Each plane permitted measuring the X or Y particle coordinates independently. The planes were divided into half-planes which did not overlap. The hodoscope elements had a cross-section of 14×12 mm, and their length was varied from 0.7 to 1.8 m in accordance with the hodoscope element position. Scintillation light was detected by FEU-84-3 photomultiplier tubes.

The GEPARD calorimeter contained 1968 cells with dimensions 75.5×75.9 mm . Each cell was a sandwich of 40 alternating Pb (3 mm) and scintillator (5 mm) layers. Thus, the total radiation length was

$21X_0$. Scintillation light from all the cell scintillators was collected by the FEU-84-3 photomultiplier tubes by means of a special light guide with wavelength shifting admixtures.

Signals from the scintillation and Cherenkov counters were used in the Level-1 trigger. The decayed-kaon trigger was formed according to the following logical formula:

$$T1 = S1 \cdot S2 \cdot S3 \cdot S4 \cdot (D1 + D2) \times \overline{C1} \cdot \overline{C2} \cdot \overline{C3} \cdot \overline{\mathrm{AC}}$$

(the signals involved in this formula were received from the detectors indicated in Fig. 1). The Level-2 trigger performed fast analysis of the amount and topology of the energy deposition in the GEPARD trigger modules.

3. EVENT RECONSTRUCTION AND SELECTION

Processing of each event recorded in the experiment began with the reconstruction of its elements, including clusters in the calorimeter and the charged particle tracks. If the topology of events corresponded to the studied decay, they were subjected to a kinematic analysis within a hypothesis suggesting certain final decay products. Based on the results of this analysis, the event was either classified as one of the decays corresponding to the given kinematic hypotheses or rejected.

3.1. Energy-Deposition Cluster in the Calorimeter

A correlated group of triggered calorimeter cells, in which the signal amplitude exceeds a certain threshold value, is traditionally called a cluster. Measurement of the total energy deposited in the cluster makes possible determination of the energy of electron (positron) or a γ-quantum passing through the GEPARD calorimeter. Calibration constants that are necessary to determine the energy from the measured signal amplitude have been found for each calorimeter cell in calibration runs with an electron beam.

The following algorithm was used in search for the clusters. Triggered calorimeter cells are ordered with respect to decreasing deposited energy. A cell with the maximum energy deposition is considered to be the cluster centre. If there are triggered cells among eight neighboring cells, they are assigned to this cluster and excluded from further consideration. The next cell with the maximum energy is chosen from the remaining cells. If its energy deposition is above 0.8 GeV, this cell is considered to be the center of a new cluster, and the whole procedure is repeated. If the energy deposition is below 0.8 GeV, the cell is added to one of the clusters found earlier (if adjacent to it) or is considered to be the initial one for a new cluster. The process is over when all the triggered cells are assigned to one of another cluster. In particular, a cluster can contain only one cell.

The total energy E_{clst} of a cluster and the coordinates of its center of gravity $(x_{\mathrm{clst}}, y_{\mathrm{clst}})$ are calculated for each cluster as follows:

$$E_{\mathrm{clst}} = \sum_{i=1}^{N_{\mathrm{clst}}} E_i, \tag{4}$$

$$x_{\mathrm{clst}} = \sum_{i=1}^{N_{\mathrm{clst}}} x_i^{\mathrm{cell}} E_i / E_{\mathrm{clst}}, \quad y_{\mathrm{clst}} = \sum_{i=1}^{N_{\mathrm{clst}}} y_i^{\mathrm{cell}} E_i / E_{\mathrm{clst}},$$

where x_i^{cell} and y_i^{cell} are the coordinates of the center of the ith calorimeter cell; E_i is the energy deposition in this cell; the summation is performed over all cells assigned to a certain cluster. The dispersion of coordinates defined by Eqs. (4) was found using a similar algorithm.

It was shown [16] that the shower coordinates defined by Eqs. (4) can be improved if the exponential behavior of the shower profile is taken into account. We elaborated and applied a special procedure to refine the coordinates of the shower origin.

A thorough analysis of the electromagnetic shower shape enabled us also to obtain corrections to the cluster energy as a function of the shower coordinates, which were recalculated with respect to the edge of the calorimeter cell. We calculated these corrections and presented them in terms of second-order polynomials in the y coordinate of the shower origin measured from the cell edge. The polynomial coefficients vary with the band number along the x axis, while the band size is fixed at $1/15$ of the width cell.

3.2. Track Reconstruction

Triggered elements of hodoscopes $H1$–$H3$ and the obtained coordinates of the cluster centers were used to reconstruct the trajectories of the decay products. To reduce the combinatorial background, tracks were considered as reconstructed if they had not less than three measurements for each of the X and Y coordinates in the $H1$–$H3$ hodoscopes and the GEPARD calorimeter.

Since there is no magnetic field in the setup, charged particle tracks are straight lines; their parameterization was selected in the following form:

$$X = a_x + b_x Z, \quad Y = a_y + b_y Z.$$

Track projections in the (X, Z) and (Y, Z) planes were reconstructed independently by combining coordinates of the triggered elements; the track parameters and the confidence level (CL) for each coordinate combination on a straight line were obtained using the least squares method. At the first stage of data processing, the uncertainties of the coordinate measurement were assumed to be identical. It enabled us to considerably reduce the processing time of possible combinations and to reject a priori unacceptable variants.

In addition to the width of the hodoscope elements, the multiple scattering in the hodoscope material contributes to the uncertainty of track coordinate determination; its influence upon the accuracy of the track coordinate measurement was studied using the Monte Carlo (MC) method. The obtained dependences were approximated with the following function

$$\sigma_i^H = \frac{h}{\sqrt{12}} + \frac{A_i}{p}, \tag{5}$$

where h is the width of the hodoscope element, p is the charged particle momentum, and A_i is the value which depends on the hodoscope number i. The simulated A_i values were used in data processing.

At the initial stage of the reconstruction, the charged particle momentum is unknown; therefore, values obtained with formula (5) at $p = 5$ GeV/c were taken to be the uncertainties in track coordinates. Subsequently, after estimating the momentum value as a result of the event kinematic fit, the track parameters were recalculated with refined values of the measurement uncertainties.

The method of processing track candidates with more than two common points is one of the important special features of the reconstruction procedure. The CL which depends on the χ^2 value and the number of points in the track was calculated for each event, and then a single candidate with the maximum CL was retained.

The following criteria were used to combine the charged particle projections into a three-dimensional track: either X and Y projections of the track pass through the same cluster in the calorimeter or neither of the projections passes through the cluster but both of them fall in the same quadrant.

3.3. Event Topology

Only those events were considered in further processing for which the hypothesis on the intersection of a charged decay particle track with the beam axis had a CL above 5%, and the intersection point (the event vertex) was inside the volume of the evacuated pipe. In addition, the reconstructed events satisfied the following selection criteria:

(i) Three clusters with the energy deposition above 1 GeV must be reconstructed in the calorimeter.

(ii) The track reconstructed using the $H1$–$H3$ hodoscopes must cross one of the clusters that is called charged, while the rest of the clusters are considered neutral.

The events which satisfied these selection criteria were subjected to kinematic fitting, which allowed us to introduce the available a priori information into their processing and to improve the estimations of the kinematic parameters of the decay particles within the assumption of the decay type.

3.4. Kinematic Fitting

The following set of the measured values was used in kinematic fitting: the γ-quantum energies and coordinates (E^{γ_i}, x^{γ_i}, y^{γ_i}), the mean energy of K meson and its track parameters (E^K, a_x^K, b_x^K, a_y^K, b_y^K), and the charged particle track parameters ($a_x^{\pm}$, $b_x^{\pm}$, $a_y^{\pm}$, $b_y^{\pm}$). The parameters of the energy-deposition clusters corrected for the transverse profile of the electromagnetic shower and for the calorimeter nonuniformity were taken as the coordinates and energies of γ-quanta and electrons. The $\pi^{\pm}$ meson energy E^{π} in $K_{\pi 2}$ and $K_{\pi 3}$ decays and the neutrino momentum $\mathbf{p}_{\nu}$ in K_{e3} decay were unknown variables.

The fitting parameter values must satisfy equations determined by the kinematics of the decay studied, including four equations corresponding to the energy-momentum conservation and one equation for the effective mass of the γ-quantum pair that is taken equal to the tabulated value of the π^0 meson mass [7]. An additional equation corresponds to the intersection of the charged track with the beam axis at point (X_V, Y_V, Z_V) and yields the following relationship between their parameters:

$$\begin{gathered}(b_x^K - b_x^{\pm})(a_y^K - a_y^{\pm}) \\ - (b_y^K - b_y^{\pm})(a_x^K - a_x^{\pm}) = 0.\end{gathered} \tag{6}$$

The direction cosines c_x^j, c_y^j, c_z^j of the γ_i particle trajectories ($i = 1, 2$) are calculated as follows:

$$c_x^{\gamma_i} = (x^{\gamma_i} - X_V)/r_i, \quad c_y^{\gamma_i} = (y^{\gamma_i} - Y_V)/r_i,$$
$$c_z^{\gamma_i} = (z_{\text{cal}} - Z_V)/r_i,$$
$$r_i = \sqrt{(x^{\gamma_i} - X_V)^2 + (y^{\gamma_i} - Y_V)^2 + (z_{\text{cal}} - Z_V)^2},$$

where z_{cal} is the Z coordinate of the electromagnetic calorimeter. For the charged particles ($j = \pi^{\pm}, K^{\pm}, e^{\pm}$), we obtain

$$c_x^j = b_x^j \Big/ \sqrt{1 + (b_x^j)^2 + (b_y^j)^2},$$
$$c_y^j = b_y^j \Big/ \sqrt{1 + (b_x^j)^2 + (b_y^j)^2},$$

$$c_z^j = 1\Big/\sqrt{1 + (b_x^j)^2 + (b_y^j)^2}.$$

The following final equations can be written for the four-momentum components and the squared effective mass of the γ-quantum pair:

$$c_x^K p^K - c_x^\pi p^\pi - \sum_{i=1,2} c_x^{\gamma_i} E^{\gamma_i} = 0, \qquad (7)$$

$$c_y^K p^K - c_y^\pi p^\pi - \sum_{i=1,2} c_y^{\gamma_i} E^{\gamma_i} = 0,$$

$$c_z^K p^K - c_z^\pi p^\pi - \sum_{i=1,2} c_z^{\gamma_i} E^{\gamma_i} = 0,$$

$$2E^{\gamma_1} E^{\gamma_2}(1 - c_x^{\gamma_1} c_x^{\gamma_2} - c_y^{\gamma_1} c_y^{\gamma_2} - c_z^{\gamma_1} c_z^{\gamma_2}) - m_{\pi^0}^2 = 0,$$

$$E^K - \sum_{i=1}^{3} E^i = 0.$$

The fitting (corrected) kinematic parameters of the decay products must obey the system of equations (6) and (7).

The corrected kinematic parameters $\mathbf{x}'$ of the decay particles were estimated using the Lagrange method of undetermined multipliers. Here, the following functional was minimized:

$$\chi^2 = (\mathbf{x} - \mathbf{x}')^T \mathbf{V}^{-1} (\mathbf{x} - \mathbf{x}') - \boldsymbol{\lambda}^T \mathbf{f}(\mathbf{x}'), \qquad (8)$$

where $\mathbf{x}$ is the vector of measured kinematic parameters of the decay particles, $\mathbf{V}$ is their covariance matrix, and $\mathbf{f}(\mathbf{x}')$ are the functions determining a multidimensional surface in the space of fitted parameters. In particular, there are, 15 measured and 15 fitted parametersfor the kinematic fit of decay $K^\pm \to \pi^\pm \pi^0$, and six kinematic equations are used, one of which is used for calculation of the charged pion energy. Hence, there are five constraints in this case (5C-fit). The hypotheses of $K^\pm \to \pi^\pm \pi^0 \pi^0$ and $K^\pm \to e^\pm \nu \pi^0$ decays correspond to 6C- and 3C-fit, respectively.

Functional (8) was minimized by means of iterations with linearization of the constraint equations and recalculation of covariance matrix of the corrected values $\mathbf{V'}$ at each iteration. The following condition was selected as a prerequisite for the convergence: reduction of the relative variation at a particular step must be such that

$$\max_i \left(|x_i - x_i'| \Big/ \sqrt{V_{ii}'} \right) < 10^{-5}.$$

The requirement imposed on the precision of validity of the constraint equations was $\leq 10^{-6}$.

4. MONTE CARLO SIMULATION

The MC simulation of the experiment was performed using the GEANT-3.21 program package [17]. In addition to a detailed description of the setup geometry, we took into account the experimental data, including the calibration coefficients for each channel of the electromagnetic calorimeter, the dependence of the particle detection efficiency in the scintillation hodoscopes on the particle coordinates, and the correlations between the spatial and angular coordinates of beam kaons and between these coordinates and the kaon momenta. The GEANT standard list of kaon decays was expanded. We modified the code so that it enabled simulating any of the known K meson decays.

The simulated and experimental data were saved in the same format and processed with the same codes for their reconstruction and analysis.

A global coordinate system was introduced to describe the setup geometry and the event reconstruction, which was determined by the following conditions:

(i) The Z axis is perpendicular to the planes of the $H1$–$H3$ hodoscopes and the GEPARD calorimeter and passes through the center of the electromagnetic calorimeter; this axis is directed along the beam particle motion (the Z axis direction does not coincide with the beam axis since the latter is inclined ∼9 mrad with respect to the horizontal plane).

(ii) The origin of the coordinate system is placedat the intersection point of the Z axis with the plane of the exit flange of the evacuated pipe.

(iii) The Y axis is directed upward vertically.

(iv) The X axis is directed so as to complete the (Y, Z) pair to the right-handed system.

The coordinates of the detectors and their elements were determined in geodetic measurements, their results were introduced into the codes of reconstruction of the real and MC events and into the codes simulating the studied decays. The analysis of variances for the reconstructed tracks and triggered elements of various detectors confirmed the adequacy of the input data. A distance from the point of the track intersection with the hodoscope plane to the center of the triggered hodoscope element was used as the variance for scintillation hodoscopes while a distance from the point of the track intersection with the front calorimeter plane to the transverse coordinates of the shower axis was used as the variance for the calorimeter.

The BH3–BH4 beam hodoscopes separated by a distance of ∼10 m and located in front of the evacuated pipe allowed measuring the parameters of the spatial and angular distribution of particles in the beam. These data were used to simulate the particle

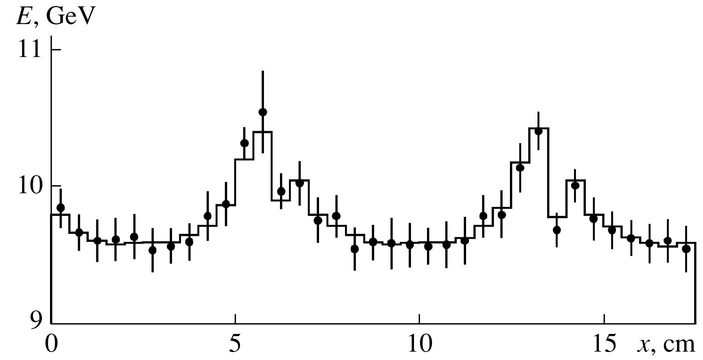

Fig. 2. Electromagnetic calorimeter response E as a function of the electron coordinate x determined with respect to the calorimeter cell edge. The points and the histogram show the experimental and simulated data, respectively.

distribution in the beam with the correlations between the particle coordinates and the directions of their trajectories taken into account.

The efficiency of the scintillation hodoscopes recording trajectories of the decay products is one of the important factors that should be taken into account in simulating the setup operation. We evaluated the efficiency by using the tracks of $\pi^{\pm}$ mesons with energies above 5 GeV from $K^{\pm} \to \pi^{\pm}\pi^0$ decays. In order to avoid uncertainties associated with detection of the e^+e^- pairs in the photon conversion at the exit flange of the evacuated pipe, we selected only single-track events. The condition of the intersection of the charged particle trajectories with the front hodoscope plane allowed the number of the cell traversed by the particle to be determined even if there was no signal from the cell. Hence, it allowed us to determine the probability of signal recording or missing. The experimental data were subdivided into sample sets corresponding to the stable operating mode of the hodoscopes; each hodoscope cell was treated as described above. The obtained tables of efficiencies were taken into account in simulating the setup operation.

5. INHOMOGENE OF THE ELECTROMAGNETIC CALORIMETER

The structure of each cell of the electromagnetic calorimeter was described in maximum detail. In particular, we took into account its size, the alternation of the lead and scintillator layers, the location and size of the light guide and the cell steel shield. The studies have shown that to a considerable extent, the calorimeter inhomogeneity is caused by the Cherenkov light emitted by the electromagnetic shower particles traversing the light guide [18]. In addition to the energy deposition in the scintillator plates ($E_{\rm sc}$), the number of the charged particles which were produced in the cascade and passed through the light guide ($N_{\rm lg}$) was also used to calculate the particle energy. Functions relating the $E_{\rm sc}$ and $N_{\rm lg}$ values to the energy of the particle absorbed in the calorimeter were obtained from the MC data for the electron beams and those of the γ-quanta of different energies as well as from the experimental data saved on the magnetic tapes during the test runs with the electron beam. A scintillation hodoscope was installed upstream of the calorimeter during these measurements, which measured the coordinates of electron striking the calorimeter cell. Thus we obtained the following formula for the energy $E_{\rm cell}$ deposited in the calorimeter cell for the simulated data

$$E_{\rm cell} = 7.48E_{\rm sc} + 0.0054N_{\rm lg}, \qquad (9)$$

where the energy $E_{\rm sc}$ is measured in GeV.

Figure 2 shows the experimental data obtained in the test run with the typical assembly of two GEPARD cells and the simulated data calculated with formula (9). It is evident that the method enables us to adequately describe the experimental data.

6. RESULTS OF SIMULATION OF $K^{\pm} \to \pi^{\pm}\pi^0$ DECAYS

Decays $K^{\pm} \to \pi^{\pm}\pi^0$ were used to verify the adequate simulation of the setup operation [12]. Figure 3 presents the distributions of the γ-quantum pairs with respect to the effective mass for each sample of the experimental and MC events from these decays; the energy of the γ-quantum was measured with the GEPARD electromagnetic calorimeter. The π^0 mass resolution appeared to be $\sim$12.3 MeV while the mean mass was 135 MeV.

Figure 4 shows the distributions with respect to kinematic variables for the experimental and simulated events from decays $K^{\pm} \to \pi^{\pm}\pi^0$. Evidently, the simulating codes adequately describe processes in the setup. The distribution over the angles between kaon

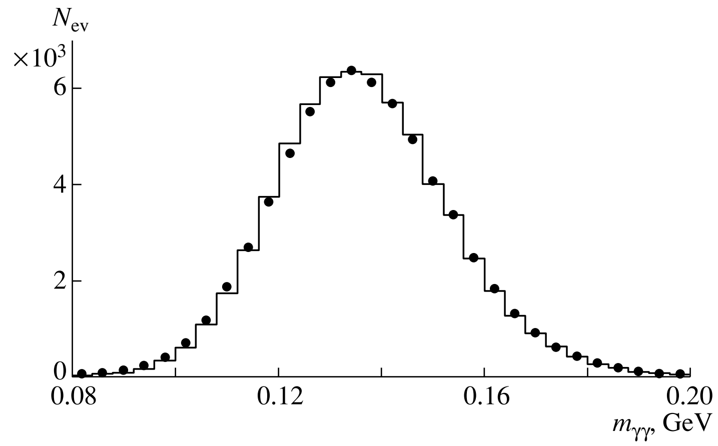

Fig. 3. Distribution of events with respect to the effective mass of γ-quantum pair from $K_{\pi 2}$ decays (the points and the histogram show the experimental and simulated data, respectively).

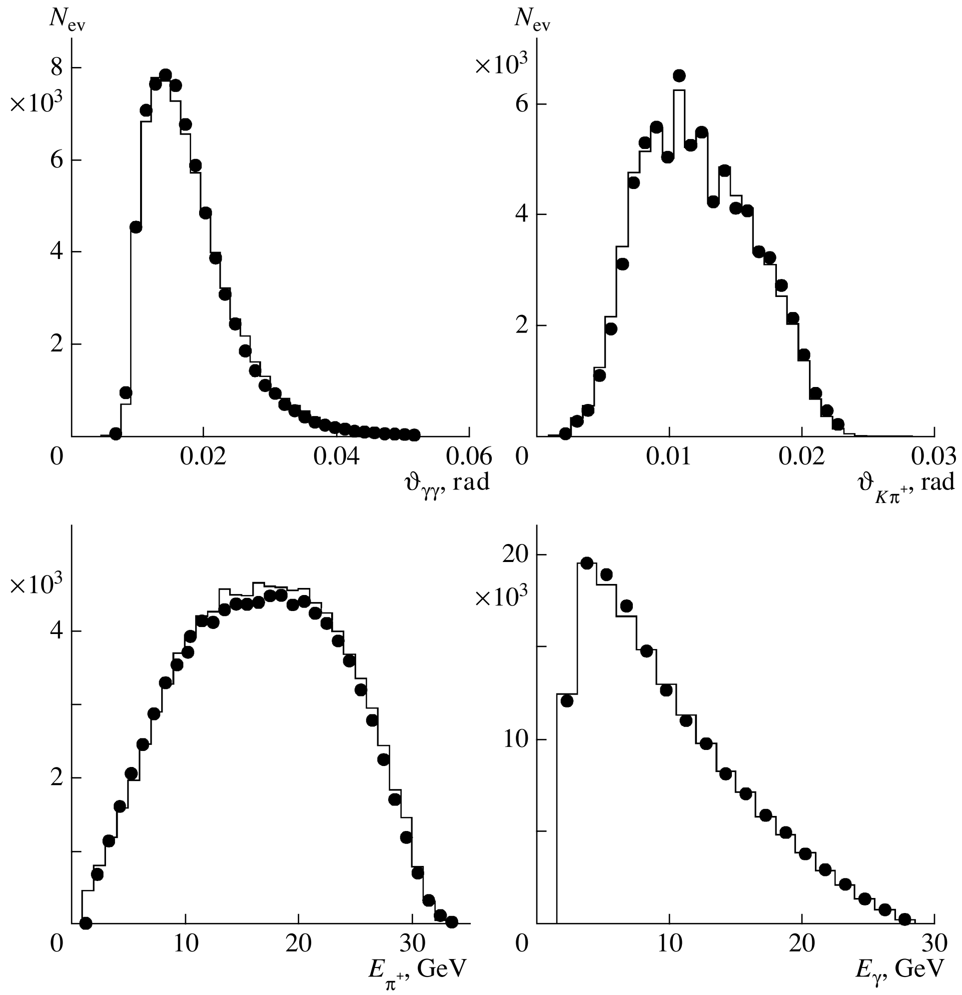

Fig. 4. Distribution of events from $K^\pm \to \pi^\pm\pi^0$ decays with respect to kinematic variables (the points and the histogram show the experimental and simulated data, respectively).

and charged pion is especially illustrative, since the structure caused by the discreetness of the $H1-H3$ hodoscope elements is quite evident.

The numbers of events obtained during complete simulation of all processes in the setup were $\sim$80M ($K \to \pi\pi^0$), $\sim$77M ($K \to e\nu\pi^0$) and $\sim$40M ($K \to \pi\pi^0\pi^0$). In simulations, we took into account additional information on some special features of the setup operation in the course of each run, including the hodoscope efficiency, the map of failure cells of the calorimeter, and so on.

7. CALIBRATION OF THE GEPARD CALORIMETER AND DETERMINATION OF THE KAON AVERAGE ENERGY

More than 8M of events with one charged and two neutral clusters were saved on the magnetic data carriers in the course of the experiment.

Two independent methods were used to calibrate the calorimeter: by irradiating each cell with a 10-GeV electron beam at the beginning of data accumulation and by means of kinematic fitting of the parameters of γ-quanta from $K^{\pm} \to \pi^{\pm}\pi^{0}$ decays. The latter procedure was carried out permanently throughout the experiment, and the final calibration values were obtained dirung in the off-line processing of the gained statistics. Both methods provide the results which are in good agreement with each other. However, an additional procedure was performed at the final stage of processing of the experimental data on K_{e3} decay in order to refine the GEPARD calibration coefficients. According to this, the calibration coefficients were varied so as to make the position of the maximum of the effective mass distribution for γ-quantum pairs from K_{e3} decay equal to the neutral pion mass indicated in PDG [7]. This procedure was applied to each statistical sample portion accumulated separately for kaon of a definite sign, the sign of the kaon charge being changed 16 times in each run.

We have refined the value of the beam kaon momentum for an experimental sets of $K^{\pm} \to \pi^{\pm}\pi^{0}$ events, assuming that none of the decay particle momenta are measured, beam kaon momentum among them (2C-fit). This procedure was applied separately to each of the above mentioned parts of statistics. The most probable value of the beam kaon momentum appeared to be 36.25 ± 0.25 GeV/c, and a bias of this value within each part of statistics did not exceed the indicated uncertainty. We also studied the dependence of the reconstructed momentum on various physical variables. This value was found to correlate with the value of the reconstructed coordinate Z_V of the decay vertex, and that was accurately reproduced by the simulation result.

Table 1. Probability (W) of reconstruction of $K_{\pi2}$, K_{e3} and $K_{\pi3}$ decays as the K_{e3} decay satisfying the selection criteria, and their expected share (V) in the real event sample set

	Simulated decay type*		
	$K \to \pi\pi^0$	$K \to e\nu\pi^0$	$K \to \pi\pi^0\pi^0$
W, %	9.07	50.91	20.87
V, %	1.897	2.535	0.367

* Note: all decays were simulated with $|M|^2 \sim$ const.

It was found in data processing that the pulse height sometimes exceeds the ADC range[1)]. The energy deposition in these cells was taken to be above the limit preset for the ADC in the algorithm of reconstruction of the cluster center-of-gravity coordinates (4), although the total cluster energy was considered uncertain. Thus, the value associated with the energy of electrons or the γ-quanta could be calculated. Hence the number of the constraint equations decreased by unity in this case.

We used $K_{\pi2}$ decays with no less than four constraint equations for the methodological studies.[2)]

8. REJECTION OF BACKGROUND PROCESSES

The result of simulation showed that the most substantial background is caused by $K_{\pi2}$ decay (see Table 1). The procedure of its suppression was subdivided into two successive stages. First kinematic fit of each event was performed within the hypothesis that particles of the final state were charged pion (a charged cluster) and γ-quanta (two neutral clusters)—that is, $K_{\pi2}$ decay occurred. If the probability of the $K_{\pi2}$ hypothesis for the given event was above 40% as a result of its kinematic fit, its further processing was stopped—that is, it was rejected. Otherwise, the event was fitted within the hypothesis that K_{e3} decay took place (second stage). Since the neutrino momentum was not measured, the selected event was fitted with three[3)] constraint equations (3C-fit).[4)] The distribution of events processed in this manner was used for the statistical analysis of the experimental data.

[1)] channel overloading

[2)] Except for the case of estimation of the beam momentum.

[3)] or less than three constraints if the ADC channels were overloaded

[4)] Here the electron energy is the energy of the charged cluster.

The $K_{\pi 3}$ events were not fitted similarly within the kinematic hypothesis of $K^\pm \to \pi^\pm \pi^0 \pi^0$. The topology of such decay is consistent with observing one charged cluster and up to four neutral clusters in GEPARD. The simulation showed that such events are efficiently rejected (see Table 1) except for those with only two of the four neutral clusters observed. The Dalitz plots of the events with two observed clusters were obtained by simulating $K_{\pi 3}$ decays with its subsequent reconstruction within the K_{e3} hypothesis. These plots were also used in the statistical analysis of experimental data.

An analysis of the experimental and simulated events showed that events with the γ-quanta passing near the window in the exit flange and near the system fixing it to the flange should be rejected. These events are caused mainly by $K_{\pi 2}$ decays. In addition, leakages of the shower particles through the GEPARD window are considerable for a noticeable part of these γ-quanta. The GEPARD window serves to allow the passage of the beam particles which have not decayed within the evacuated pipe volume.

Special features of the kinematics of the two-particle decay make it possible to introduce sufficiently effective criteria for rejecting events of $K_{\pi 2}$ decay. Let the transverse momentum of π^0-meson (q_t) be measured from the axis perpendicular to the plane determined by the beam kaon momentum and the unit vector collinear with the charged particle vector ($\mathbf{n}_+$). Then, the transverse momentum of π^0 meson is

$$q_t = \frac{\mathbf{p}_{\text{beam}} \times \mathbf{n}_+}{|\mathbf{p}_{\text{beam}}|} \cdot \mathbf{p}_{\pi^0}. \tag{10}$$

For example, the constraint $|q_t| \geq |q_t^{\text{thr}}| \sim 0.05$ GeV$/c$ allows reducing the background from $K_{\pi 2}$ to 14% of the selected statistical sample, but its size decreases to almost one-third in this case. For this reason, the indicated criterion was used only in the methodological studies.

9. THE MAIN SELECTION CRITERIA OF EVENTS FROM DECAY K_{e3}

These are the event selection criteria chosen to be the main ones:

(1) The conditions of the first and the second level triggers are met.

(2) The topology of the event complies with the requirements from subsection 2.3.

(3) The number of measured points is no less than three per track.

(4) The energies of the γ-quanta[5)] are above 1 GeV.

(5) The electron (positron) energy is above 3 GeV.

(6) The missing energy of the decay is above 12 GeV.

(7) The event vertex Z_V is sufficiently far from the entrance and exit flanges of the evacuated pipe ($-40 < Z_V < -20$ m).

(8) The γ-quantum trajectories do not pass through the region of the exit flange window and through the system fixing it on the flange.

(9) The probability of the event to occur via $K \to \pi\pi^0$ decay is below 40%.

(10) The hypothesis of $K \to e\nu\pi^0$ decay with two or three constraint equations (2C- or 3C-fit) is plausible.

Table 1 depicts the probability of meeting the mentioned selection criteria for the events from various decays.

10. DATA ANALYSIS AND RESULTS

10.1. Fitting of Dalitz Plot

The Dalitz plots of the events observed in the experiment and reconstructed as K_{e3} decay were fitted to the following expression

$$\frac{1}{N}\frac{d^2N}{dydz} = \alpha\rho^{K_{e3}}(y,z) + \beta\rho^{K_{\pi 2}}(y,z) + (1-\alpha-\beta)\rho^{K_{\pi 3}}(y,z), \tag{11}$$

where

$$y = \frac{2E_e}{m_K}, \qquad z = \frac{2E_{\pi^0}}{m_K}$$

are the energies of electron and pion, respectively, in the rest frame of decaying kaon. The functions $\rho^{K_{e3},K_{\pi 2},K_{\pi 3}}(y,z)$ are determined from the MC events for K_{e3}, $K_{\pi 2}$, and $K_{\pi 3}$ decays. These events are processed with a sequence of codes developed to reconstruct the kinematic parameters of K_{e3} decay. Thus, for $\rho^{K_{e3}}(\mathbf{x})$ of K_{e3} decays[6)], we have

$$\rho^{K_{e3}}(\mathbf{x}) = \int G(\mathbf{x},\mathbf{x}')\rho'^{K_{e3}} d\mathbf{x}',$$

where $G(\mathbf{x},\mathbf{x}')$ is the operator which transforms the kinematic variables $\mathbf{x}'$ into $\mathbf{x}$. The values of $\mathbf{x}'$ variables are obtained in decays K_{e3}, or $K_{\pi 2}$, or $K_{\pi 3}$ simulated with probability densities $\rho'^{K_{e3}}$, or $\rho'^{K_{\pi 2}}$, or $\rho'^{K_{\pi 3}}$, respectively. The $\rho'^{K_{e3}} = \rho'^{K_{e3}}(y',z';\lambda,f_T,f_S)$ function is determined by relation (2) with radiation corrections to K_{e3} decay taken into account; $\rho'^{K_{\pi 2}}$ corresponds to the uniform distribution throughout the whole phase space of $K_{\pi 2}$ decay, and $\rho'^{K_{\pi 3}}$

[5)]This threshold was increased up to 2 GeV to estimate the systematic error uncertainties.

[6)]The expressions for all other kaon decays are similar.

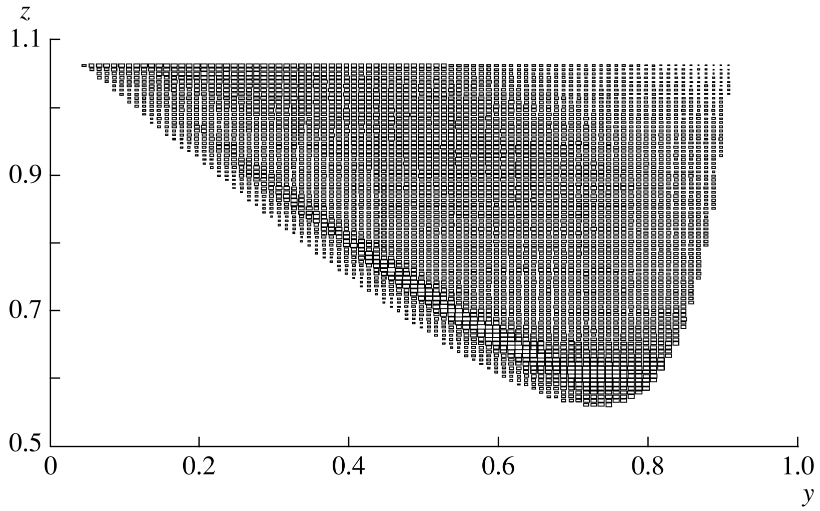

Fig. 5. Two-dimensional Dalitz plot of selected events.

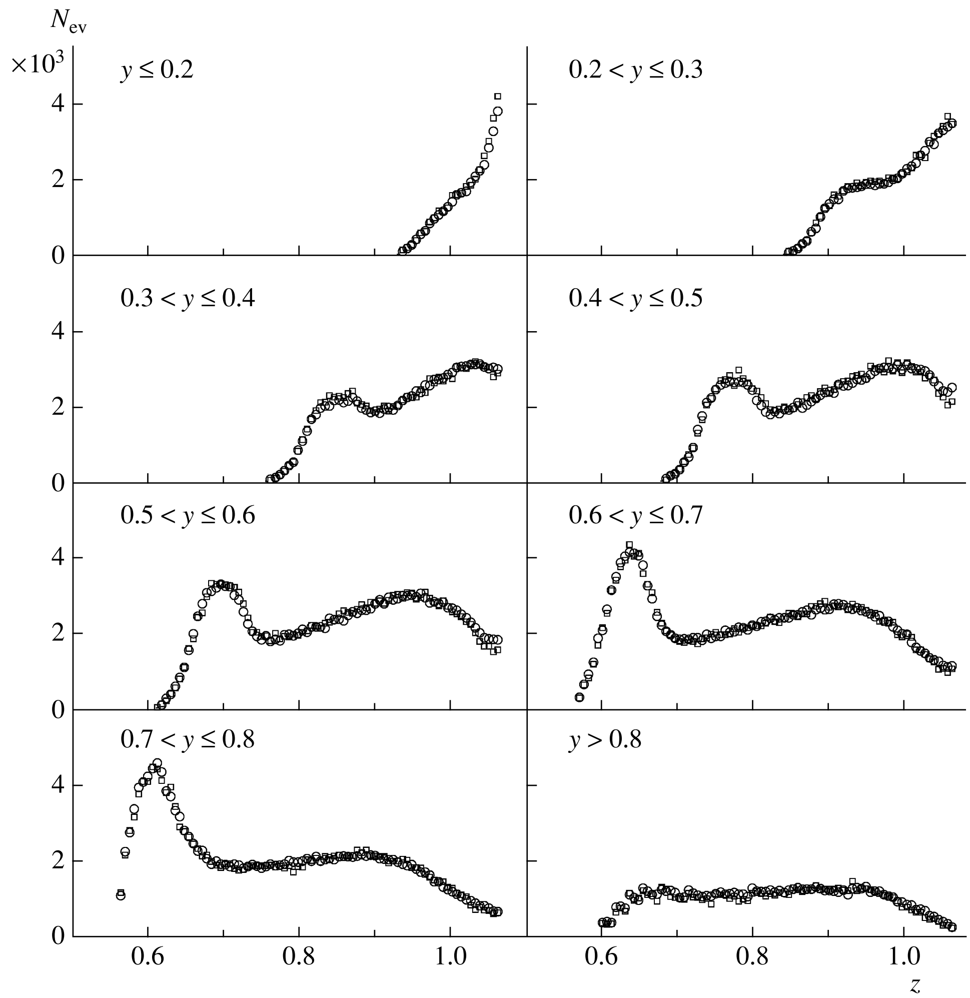

Fig. 6. Distributions of real (○) and simulated (□) events corresponding to expression (11) with parameters obtained in minimization of the functional $-\ln L$ (12).

Table 2. Dalitz distribution of events obeying the selection criteria (Section 9) fitted to expression (11)

$\lambda_+, 10^{-3}$	$f_T(0)/f_+(0), 10^{-2}$	$f_S(0)/f_+(0), 10^{-2}$	α, %	β, %	$1-\alpha-\beta$, %	χ^2/NDF
30.44 ± 0.83	0	0	68.63 ± 0.10	30.35 ± 0.09	1.02	4838/4487
30.21 ± 0.83	5.0 [2]	1.5 [2]	68.65 ± 0.10	30.34 ± 0.09	1.01	4839/4487
30.43 ± 0.83	-1.2 [1]	-0.37 [1]	68.63 ± 0.10	30.35 ± 0.09	1.02	4838/4487

depends on the standard variables u and v and the parameters g, h, k [7]:

$$\rho'^{K_{\pi 3}}(u, v; g, h, k) \sim 1 + gu + hu^2 + kv^2.$$

The values of the parameters $g = 0.6259$, $h = 0.0551$, and $k = 0.0082$ were taken from our publication [13].

Hence, α, β, λ, f_T, and f_S are fitted parameters. They are estimated using the maximum likelihood method; the logarithm of the likelihood function is

$$\ln L = \sum_{i}^{r} \left[n_i \ln \frac{m_i}{n_i} - m_i + n_i \right], \quad (12)$$

where r is the number of the histogram bins; n_i and m_i are the quantities of the observed and simulated events in the ith bin of the Dalitz plot. We used the MINUIT code [19] to search for the extremum of functional (12). Expression (11) was recalculated at each iteration in the search for the extremum.

10.2. Estimation of the Dalitz Plot Parameters

The parameters of expression (11) were estimated by the analysis of the Dalitz plot for the events which obeyed the selection criteria from Section 9. The total number of selected events appeared to be $\sim$1.08M in spite of the imposed stringent requirements, while the number of the simulated events was $\sim$0.572M (K_{e3}), $\sim$82k ($K_{\pi 2}$), and $\sim$4.3k ($K_{\pi 3}$). Figure 5 shows the distribution of selected events over the Dalitz variables. Table 2 presents the estimates of the fitted parameters[7)]. The estimates were found with $f_T(0)/f_+(0)$ and $f_S(0)/f_+(0)$ fixed, in particular with their values indicated in [1, 2]. We should note that the χ^2 values are practically identical for all the fitting versions just as it is expected in agreement with the conclusions presented in the Appendix. The quality of fitting the two-dimensional Dalitz plot is illustrated in Fig. 6 which shows separate "bands" versus y for the real and simulated events.

7) $\lambda' = 0$ everywhere.

10.3. Systematic Uncertainties

The stability of the beam and detector parameters was thoroughly controlled in the course of accumulations. Although all measures were taken to provide the identical properties of the beams of positively and negatively charged kaons, the mean values of the angles at which they entered the setup could differ by $\Delta a_x = 5$ μrad and $\Delta a_y = 7$ μrad, and their mean energies could differ by 250 MeV. The systematic errors caused by these deviations were estimated by means of splitting the statistical sample with respect to the sign of beam kaons.

In order to take into account the influence of the boundary regions on the Dalitz plot, we did not consider the events which lay in the boundary bands; we also changed the thresholds for the measured energies of the decay particles, on the missing energy, the transverse momentum value, and other parameters. The most significant sources of the systematic error of the results and their contributions are presented in Table 3.

We also analyzed other possible sources of the systematic error, including the instability of the magnetic calorimeter calibration and of the scintillation hodoscope efficiencies with time, the influence of the Earth magnetic field on the beams of the particles of different signs, and the difference in the interaction cross sections of π^+ and π^- mesons with matter. The total contribution of these factors to the systematic uncertainty of the estimates appeared to be insignificant [12].

11. CONCLUSIONS

Processing of the data on decays of charged kaons obtained in the experiments with the KMN setup at IHEP enabled us to extract $\sim$1.08M candidate decays $K^{\pm} \to e^{\pm}\nu\pi^0$. The analysis of the Dalitz plots for the mentioned decays allowed obtaining the following estimate for the linear slope of the charged form factor:

$$\lambda_+ = [30.44 \pm 0.83(\text{stat.}) \pm 0.74(\text{syst.})] \times 10^{-3},$$

which is somewhat above the value $[27.74 \pm 0.47(\text{stat.}) \pm 0.32(\text{syst.})] \times 10^{-3}$ obtained in the ISTRA+ experiment by use of a statistical sample of

~0.9M events from decay $K^- \to e^-\nu\pi^0$ with only the slope λ_+ fitted [1]. Our estimate is also in good agreement with the values λ_+ for decays $K^0 \to \pi^{\pm}e^{\mp}\nu$, obtained in the NA48 and KLOE experiments under the identical conditions (~5.6M [2] and ~2M [5], respectively) with allowance for the difference in the masses of charged and neutral pions:

$$\lambda_+(\mathrm{NA48})\left(\frac{m_{\pi^\pm}}{m_{\pi^0}}\right)^2 = (30.8 \pm 0.4) \times 10^{-3},$$

$$\lambda_+(\mathrm{KLOE})\left(\frac{m_{\pi^\pm}}{m_{\pi^0}}\right)^2 = (30.6 \pm 0.5) \times 10^{-3}.$$

ACKNOWLEDGMENTS

We are grateful to the IHEP headquarters for their support of the experiment; to V.N. Mikhailin for his assistance in the construction and operation of the setup; and to Yu.V. Mikhailov, A.N. Sytin, and V.A. Sen'ko for their help in manufacturing the electronics. We thank the staff of the Accelerator Department and the Beam Division who provided high-quality operation of the accelerator complex, beam extraction system, and the beam channels nos. 8 and 23. We appreciate the assistance of I.N. Belyakov, Yu.G. Nazarov, A.N. Romadanov, and I.V. Shvabovich in the detector construction.

This study was supported in part by the Russian Foundation for Basic Research (project nos. 05-02-17614 and 06-02-16605).

APPENDIX

SIMPLE MODEL

Let the number of events n in a single bin of the Dalitz plot, be a random variable with the Poisson distribution, that is,

$$f(n;\theta) = \frac{\mu^n}{n!}e^{-\mu}. \tag{A.1}$$

Here, the function $\mu = \mu(\mathbf{x};\theta)$ depends on the set of the Dalitz variables $\mathbf{x}$ and on the multidimensional parameter θ. Then, the Fischer information matrix for the ith bin is calculated as follows [20]

$$M_f\left[\frac{\partial \ln f}{\partial\theta_l}\frac{\partial \ln f}{\partial\theta_k}\right] = \frac{1}{\mu}\frac{\partial\mu}{\partial\theta_l}\frac{\partial\mu}{\partial\theta_k} \tag{A.2}$$
$$= \frac{\partial \ln\mu}{\partial\theta_l}\frac{\partial \ln\mu}{\partial\theta_k}\mu(\mathbf{x}_i;\theta).$$

Therefore, the information for the whole histogram is

$$I_{lk} = \sum_{i=1}^{r}\frac{\partial \ln\mu}{\partial\theta_l}\frac{\partial \ln\mu}{\partial\theta_k}\mu(\mathbf{x}_i;\theta), \tag{A.3}$$

where r is the total number of the histogram bins. Supposing that

$$\mu \sim \frac{\rho^{K_{e3}}(\mathbf{x};\theta)}{\int \rho^{K_{e3}}(\mathbf{x};\theta)d\mathbf{x}}, \tag{A.4}$$

where $\rho^{K_{e3}}$ complies with expression (2), we calculated the elements of the Fischer information matrix at θ[8] as follows:

$$\lambda = 24.85 \times 10^{-3}, \quad f_T = -1.2 \times 10^{-2}, \tag{A.5}$$
$$f_S = -0.3 \times 10^{-2}.$$

The Kullback-Leibler distance[9] defined as

$$r[f_{\theta_1}, f_{\theta_2}] = \int \ln\frac{f(x;\theta_1)}{f(x;\theta_2)}f(x;\theta_1)dx \tag{A.6}$$
$$= M_{\theta_1}\left[\ln\frac{f(x;\theta_1)}{f(x;\theta_2)}\right],$$

measures the difference between the functions $f(x;\theta_1)$ and $f(x;\theta_2)$. It plays an important role in mathematic statistics, particularly in the theory of estimators and the theory of statistical inference. The following relation has been shown to be valid (see [20, 21] for example):

$$\lim_{\Delta\to 0}\frac{r[f_\theta, f_{\theta+\Delta\omega}]}{\Delta^2} = \frac{1}{2}\omega I(\theta)\omega^T, \tag{A.7}$$

where ω is some unit vector which is arbitrarily orientated in the space of the θ parameters; $I(\theta)$ is the Fischer information matrix calculated with the preset values of the θ parameter.

Hence, the following relation is valid for a line of equal level $r[f_{\theta_1}, f_{\theta_2}] = \mathrm{const}$

$$\Delta_\lambda : \Delta_{f_T} : \Delta_{f_S} = \frac{1}{\sqrt{I_{11}}} : \frac{1}{\sqrt{I_{22}}} : \frac{1}{\sqrt{I_{33}}}$$

Table 3. Sources of systematic uncertainties and estimates of their values (δ)

Source	$\delta, 10^{-3}$
Variation of the size of rejected boundary region	± 0.16
Variation of γ-quantum energy threshold (>1.5 GeV)	± 0.69
Variation of the beam kaon sign	± 0.35
Variation of the size and the location of the beam kaon decay volume	± 0.34
Total systematic uncertainty of results	± 0.74

[8] These are the mean values for the international data on K_{e3} decays from PDG [7].

[9] or the Kullback-Leibler information (see [21] for example)

under the condition that only one of the parameters is varied while all the rest of them are fixed. With the values (A.5), we obtain the following estimates from (A.3) and (A.4)

$$\Delta_\lambda : \Delta_{f_T} : \Delta_{f_S} = 0.411 : 112 : 26.7 \qquad \text{(A.8)}$$
$$= 1 : 2.73 \times 10^2 : 0.65 \times 10^2,$$

which implies that the scales of λ and f_T variations differ more than by a factor of 270 and the distinction between the λ and f_S scales is almost 70-fold if the considered region of the parameters is a vicinity of the point with the coordinates close to the mean international values of λ, f_T, and f_S [7]. Thus, it should be expected that the hypotheses with θ and $\theta + \Delta\omega$ will be indistinguishable within the maximum likelihood method for the sample size $N \sim 10^6$ for any $\theta = (\lambda, f_T, f_S)$ values lying inside the cube with sides of $\Delta_\lambda \sim 0.4 \times 10^{-3}$, $\Delta_{f_T} \sim 112 \times 10^{-3}$, and $\Delta_{f_S} \sim 26 \times 10^{-3}$. It should be emphasized that the inclusion of any additional information into the likelihood function (12) can change considerably the estimates and the conclusions obtained here.

In conclusion, note that the estimates of the parameter correlations also obtained within the Fischer information matrix (A.3) are consistent with the values

$$\rho_{\lambda f_T} = -0.167, \quad \rho_{\lambda f_S} = 0.331, \quad \rho_{f_T f_S} = -0.681.$$

REFERENCES

1. O. P. Yushchenko et al. (ISTRA + Collab.), Phys. Lett. B **589**, 111 (2004) [hep-ex/0404030].
2. A. Lai et al. (NA48 Collab.), Phys. Lett. B **604**, 1 (2004) [hep-ex/0410065].
3. A. Lai et al. (NA48 Collab.), Phys. Lett. B **647**, 341 (2007) [hep-ex/0703002].
4. T. Alexopoulos et al. (KTeV Collab.), Phys. Rev. D **70**, 092007 (2004).
5. F. Ambrosino et al. (KLOE Collab.), Phys. Lett. B **636**, 166 (2006) [hep-ex/0601038].
6. A. S. Levchenko et al. (E246 KEK—PS Collab.), Yad. Fiz. **65**, 2294 (2002) [Phys. At. Nucl. **65**, 2232 (2002)] [hep-ex/0111048].
7. W.-M. Yao et al., J. Phys. G **33**, 1 (2006).
8. M. V. Chizhov, Phys. Lett. B **381**, 359 (1996).
9. V. Bytev, E. Kuraev, A. Baratt, and J. Thompson, Eur. Phys. J. C **27**, 57 (2003); Eur. Phys. J. C **34**, 523 (2004).
10. V. Cirigliano, H. Neufeld, and H. Pichl, Eur. Phys. J. C **35**, 53 (2004).
11. P. Lichard, Phys. Rev. D **60**, 093012 (1999) [hep-ph/9903233]; Phys. Rev. D **55**, 5385 (1997).
12. G. A. Akopdzhanov et al., Eur. Phys. J. C **40**, 343 (2005) [hep-ex/0406008]; G. A. Akopdzhanov et al., Yad. Fiz. **68**, 1014 (2005) [Phys. At. Nucl. **68**, 948 (2005)].
13. G. A. Akopdzhanov et al., Pis'ma Zh. Éksp. Teor. Fiz. **82**, 771 2005) [JETP Lett. **82**, 675 (2005)].
14. V. V. Ammosov et al., Preprint No. 98-2 Inst. Fiz. Vysok. Énerg. (Protvino, 1998).
15. M. V. Akopyan et al., Preprint No. 86-129 Inst. Fiz. Vysok. Énerg. (Serpukhov, 1986); G. A. Akopdzhanov et al., Preprint No. 2007-20 Inst. Fiz. Vysok. Énerg. (Protvino, 2007).
16. G. A. Akopdjanov et al., Nucl. Instrum. Methods Phys. Res. **140**, 441 (1977).
17. CERN Program Library Long Writeup, W5013 (CERN, 1993).
18. R. N. Krasnokutsky et al., Preprint No. 84-182, Inst. Fiz. Vysok. Énerg. (Serpukhov, 1984).
19. F. James, CERN Program Library, D506 (CERN, 1994).
20. A. A. Borovkov, *Mathematical Statistics* (Nauka, Moscow, 1984; Gordon and Breach, Amsterdam, 1998).
21. S. Zacks, *Theory of Statistical Inference* (Wiley, New York, 1971; Mir, Moscow, 1975).